Biaxial Normal Strength Behavior in the Axial-Transverse Plane for Human Trabecular Bone—Effects of Bone Volume Fraction, Microarchitecture, and Anisotropy

Arnav Sanyal[1]
Orthopaedic Biomechanics Laboratory,
Department of Mechanical Engineering,
University of California,
Berkeley, CA 94720
e-mail: arnavsanyal@berkeley.edu

Tony M. Keaveny[2]
Orthopaedic Biomechanics Laboratory,
Department of Mechanical Engineering,
University of California,
Berkeley, CA 94720;
Department of Bioengineering,
University of California, Berkeley, CA 94720
e-mail: tmk@me.berkeley.edu

The biaxial failure behavior of the human trabecular bone, which has potential relevance both for fall and gait loading conditions, is not well understood, particularly for low-density bone, which can display considerable mechanical anisotropy. Addressing this issue, we investigated the biaxial normal strength behavior and the underlying failure mechanisms for human trabecular bone displaying a wide range of bone volume fraction (0.06–0.34) and elastic anisotropy. Micro-computed tomography (CT)-based nonlinear finite element analysis was used to simulate biaxial failure in 15 specimens (5 mm cubes), spanning the complete biaxial normal stress failure space in the axial-transverse plane. The specimens, treated as approximately transversely isotropic, were loaded in the principal material orientation. We found that the biaxial stress yield surface was well characterized by the superposition of two ellipses—one each for yield failure in the longitudinal and transverse loading directions—and the size, shape, and orientation of which depended on bone volume fraction and elastic anisotropy. However, when normalized by the uniaxial tensile and compressive strengths in the longitudinal and transverse directions, all of which depended on bone volume fraction, microarchitecture, and mechanical anisotropy, the resulting normalized biaxial strength behavior was well described by a single pair of (longitudinal and transverse) ellipses, with little interspecimen variation. Taken together, these results indicate that the role of bone volume fraction, microarchitecture, and mechanical anisotropy is mostly accounted for in determining the uniaxial strength behavior and the effect of these parameters on the axial-transverse biaxial normal strength behavior per se is minor. [DOI: 10.1115/1.4025679]

Keywords: multiaxial failure, anisotropy, normalize, finite element analysis, bone strength

1 Introduction

During both habitual and traumatic loading, trabecular bone is often subjected to biaxial loads, i.e., loads acting simultaneously along and transverse to the principal trabecular orientation. During gait loading, as a result of the direct action of the obliquely oriented compressive joint contact force and the associated bending of the femoral neck, the longitudinal trabeculae all the way from the femoral head to the medial femoral cortex are loaded primarily in compression whereas the corresponding transverse trabeculae in this region are loaded primarily in tension [1]. A similar biaxial loading pattern is also observed during a fall to the side on the greater trochanter, but with the tension-compression patterns reversed [2]. The biaxial strength behavior of trabecular bone is, therefore, potentially relevant to both bone adaptation under habitual loading and to whole-bone failure under traumatic loading. Concerning the latter, due to the increased structural and mechanical anisotropy of osteoporotic trabecular bone [3–6], it has been proposed that increased mechanical anisotropy may be an independent risk factor for hip fracture [7], although understanding of this issue remains incomplete.

Despite much previous research on the multiaxial behavior of bone, the biaxial failure characteristics of human trabecular bone remain unclear for bone having a low bone volume fraction, in which the degree of mechanical anisotropy can be high. A fabric-based, ellipsoidal, Tsai–Wu-type of failure criterion has been formulated for trabecular bone [8]. However, triaxial compression experiments on bovine tibial bone did not support the quadratic ellipsoidal shape of this criterion [9] and axial-torsion experiments have pointed instead to a cellular-solid-type criterion having a nonellipsoidal shape [10]. Nonlinear micro-CT based finite element simulations on bovine [11] and human [12] trabecular bone—all having high bone volume fraction—provided further evidence of the need for a multiaxial criterion that is not ellipsoidal in shape, due primarily to the different failure mechanisms associated with the different loading directions. More recently, experiments and finite element simulations were performed to fit a piecewise quadratic Hill's criterion [13] and a ellipsoidal Tsai–Wu failure criterion [14], all as a function of bone volume fraction and fabric-based morphological anisotropy. However, since these experiments and simulations only included the minimum number of load cases required mathematically to formulate

[1]Corresponding author.
[2]Please address all reprint requests to Tony M. Keaveny.

Contributed by the Bioengineering Division of ASME for publication in the Journal of Biomechanical Engineering. Manuscript received July 9, 2013; final manuscript received September 23, 2013; accepted manuscript posted October 14, 2013; published online November 6, 2013. Assoc. Editor: Kristen Billiar.

Table 1 Correlation coefficients for the five ellipse parameters for each of the longitudinal and transverse yield ellipses, the four uniaxial strengths, and the five ellipse parameters for each of the normalized longitudinal and transverse yield ellipses, with bone volume fraction (BV/TV), elastic anisotropy (EA), and a variety of microarchitecture parameters [19], for the n = 15 specimens analyzed. Bold values have $p < 0.05$.

Variable	Biaxial Yield Strength										Uniaxial Yield Strength				Normalized Biaxial Yield Strength									
	Longitudinal Ellipse					Transverse Ellipse					Longitudinal		Transverse		Longitudinal Ellipse					Transverse Ellipse				
	a	b	h	k	ϕ	a	b	h	k	ϕ	Tens	Comp	Tens	Comp	a	b	h	k	ϕ	a	b	h	k	ϕ
BV/TV	**0.99**	**0.96**	**−0.99**	**−0.91**	0.40	**0.99**	**0.91**	**−0.98**	**−0.89**	**0.59**	**0.99**	**0.99**	**0.91**	**0.90**	−0.32	**−0.71**	**0.77**	0.01	**0.56**	−0.47	**−0.56**	0.22	0.20	0.40
EA	−0.37	**−0.55**	0.36	**0.59**	**−0.78**	−0.33	**−0.61**	0.49	**0.60**	**−0.68**	−0.34	−0.37	**−0.62**	**−0.61**	**0.82**	0.29	−0.45	−0.15	**−0.67**	0.19	**0.56**	0.27	**−0.61**	0.10
SMI	**−0.90**	**−0.86**	**0.89**	**0.82**	−0.45	**−0.88**	**−0.83**	**0.88**	**0.82**	**−0.64**	**−0.90**	**−0.90**	**−0.83**	**−0.82**	0.40	**0.63**	**−0.72**	−0.06	**−0.62**	**0.57**	**0.56**	−0.30	−0.08	**−0.56**
Tb.Th	**0.87**	**0.77**	**−0.88**	**−0.69**	0.02	**0.89**	**0.67**	**−0.82**	**−0.66**	0.24	**0.88**	**0.87**	**0.68**	**0.66**	−0.01	**−0.60**	**0.58**	−0.21	0.22	−0.27	−0.39	0.12	0.05	0.28
Tb.N	**0.94**	**0.92**	**−0.94**	**−0.89**	0.51	**0.93**	**0.89**	**−0.93**	**−0.88**	**0.69**	**0.94**	**0.94**	**0.90**	**0.89**	−0.42	**−0.70**	**0.78**	0.09	**0.66**	**−0.55**	**−0.59**	0.26	0.19	0.47
Tb.Sp	**−0.84**	**−0.77**	**0.84**	**0.71**	−0.42	**−0.84**	**−0.72**	**0.80**	**0.70**	**−0.59**	**−0.84**	**−0.84**	**−0.73**	**−0.72**	0.34	**0.76**	**−0.87**	−0.20	**−0.55**	**0.58**	**0.58**	−0.50	−0.14	**−0.54**
DA	0.36	0.16	−0.35	−0.05	−0.40	0.37	0.08	−0.25	−0.05	−0.15	0.39	0.35	0.10	0.07	0.26	−0.09	0.10	−0.31	−0.09	−0.39	−0.07	0.05	−0.41	0.37
Conn-Dens.	**0.73**	**0.70**	**−0.72**	**−0.68**	0.43	**0.71**	**0.68**	**−0.72**	**−0.67**	**0.56**	**0.72**	**0.72**	**0.68**	**0.67**	−0.37	**−0.56**	**0.64**	0.31	0.51	−0.49	**−0.52**	0.19	0.36	0.25
Tb.Th.SD	**0.71**	**0.56**	**−0.72**	−0.47	−0.22	**0.74**	0.44	**−0.64**	−0.42	0.02	**0.71**	**0.70**	0.42	0.40	0.17	**−0.62**	0.51	−0.25	−0.01	−0.23	−0.34	0.24	−0.11	0.29
Tb.Sp. SD	**−0.66**	**−0.60**	**0.66**	**0.53**	−0.37	**−0.65**	**−0.55**	**0.62**	**0.53**	−0.50	**−0.66**	**−0.65**	**−0.57**	**−0.55**	0.34	**0.69**	**−0.82**	−0.31	−0.46	**0.62**	**0.54**	**−0.62**	−0.10	**−0.53**

Note: DA = degree of anisotropy, SMI = structure model index, Tb.Th = trabecular thickness, Tb.N = trabecular number, Tb.Sp = trabecular separation, Conn-Dens. = connectivity density, Tb.Th.SD = standard deviation of trabecular thickness, Tb.Sp.SD = standard deviation of trabecular separation.

a quadratic criterion—and given the aforementioned evidence from the prior triaxial compression experiments on bovine tibial bone [9]—it still remains unclear if the full biaxial failure envelope is indeed ellipsoidal in nature or if some alternative description would be more appropriate. We, therefore, sought to extend this previous research by further exploring the biaxial yield stress behavior of human trabecular bone in the axial-transverse plane, in which we spanned a wide range of loading conditions and focused on accounting also for a wide range of bone volume fraction, mechanical anisotropy, and microarchitecture.

2 Methods

We analyzed 15 specimens of morphologically diverse, human trabecular bone (cadaver age = 63 ± 12, 48–79; 4 female, 10 male) taken from four anatomic sites: vertebral body (n = 4), femoral neck (n = 7), greater trochanter (n = 2), and proximal tibia (n = 2). These specimens, taken from prior studies in our laboratory [15,16] were machined as 8 mm diameter cylindrical cores along their principal material orientation and were scanned using either micro-CT (Scanco Medical AG, Brüttisellen, Switzerland) at a voxel size of 10 μm [17] or serial milling at 22 μm [18]. The micro-CT images were down-sampled to 20 μm using region-averaging technique, and the resulting grayscale images at 20–22 μm were segmented to match the experimentally measured bone volume fraction. A 5 mm cube was virtually extracted from the central portion of these images, and the trabecular microarchitecture parameters [19] (listed in Table 1) were calculated (Skyscan: CTAn software); the Euler angles of misalignment were also calculated by conducting six uniaxial linear elastic finite element analyses [20]. The angle of misalignment of each cube specimen was confirmed to be within ±10 deg, ensuring that the axes of the extracted cube specimens were what we considered to be adequately aligned with the principal material coordinate system.

Micro-CT images of the cube specimens, at 20–22 μm resolutions, were then used to generate finite element models by converting each cubic voxel into an eight-noded brick element. First, linear elastic analysis was performed on each specimen to calculate the elastic modulus in the longitudinal (E_L) and the two transverse directions (E_{T1},E_{T2}). The percentage deviation from transverse isotropy ($\%DEV = 100\ (E_{T1} - E_{T2})/E_{T1}$) was 11.1 ± 7.7% for the 15 specimens, which we considered an acceptable error in assuming transverse isotropy of the specimens. Thereafter, the transverse direction for mechanical loading was chosen randomly for further analysis, and the elastic anisotropy (EA) was defined as the ratio of the uniaxial moduli in the two directions ($EA = E_L/E_T$).

For all the finite element models, all elements were assigned the same hard-tissue material properties having an isotropic elastic modulus of 18.0 GPa, a Poisson's ratio of 0.3, and a rate-independent nonlinear constitutive model with both elastic-plastic material and geometric kinematic nonlinearities [21]. In the constitutive model, tissue-level failure was defined using a von Mises yield criterion modified by a pseudo kinematic hardening parameter to account for the tension-compression strength asymmetry of the bone tissue. The tissue-level yield strains of 0.33% in tension and −0.81% in compression were chosen based on a prior calibration study [22]. This particular implementation has been shown to produce excellent agreement of the apparent-level 0.2% offset yield strength ($R^2 = 0.96$) with values obtained from experiments for uniaxial testing [22,23].

For each cube specimen, 18–20 separate analyses were performed, each analysis representing a uniaxial or biaxial loading state. For the uniaxial simulations, an unconstrained roller displacement boundary condition was applied in the longitudinal or transverse direction, producing an apparent-level state of uniaxial stress. For the biaxial simulations, displacement boundary conditions were applied in both the longitudinal and the chosen transverse directions; the third direction was left unconstrained,

Table 2 Power law regressions relating the four uniaxial yield strengths with bone volume fraction (BV/TV) and elastic anisotropy (EA) for n = 15 specimens analyzed. (p < 0.001 for all regressions).

	c (BV/TV)^{m1}(EA)^{m2}				
	c	$m1$	$m2$	R^2	CV(%)
Longitudinal tension (σ^y_{LT})	81.2	1.53	0	0.99	9.60
Longitudinal compression (σ^y_{LC})	183	1.73	0	0.99	9.99
Transverse tension (σ^y_{TT})	76.3	1.33	−1.07	0.99	11.2
Transverse compression (σ^y_{TC})	164	1.41	−1.30	0.99	10.3

Note: CV = coefficient of variation (ratio of the RMSE to the mean of the dependent variable).

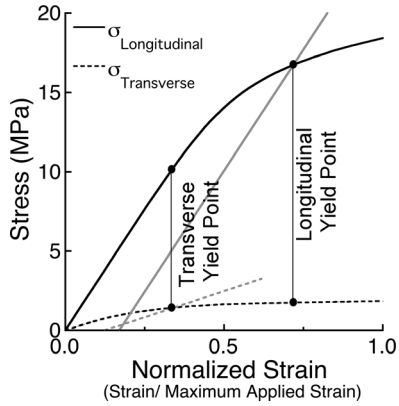

Fig. 1 Definition of the chronological yield point. This graph depicts the stress-normalized strain responses in the longitudinal (solid line) and transverse (dotted line) directions for a single specimen loaded biaxially in the longitudinal and transverse directions. The normalized strains occur at the same instant in time for both responses. For this loading, the ratio of maximum applied strain in the longitudinal to transverse direction was 0.73, and yielding first occurred along the transverse direction, which defined the chronological yield point.

thereby producing a biaxial stress state in the principal material coordinate system. Each biaxial simulation was defined by a unique ratio of the maximum applied strain in the longitudinal and transverse directions, for a total of 14–16 such biaxial loading cases. All analyses were performed using a highly scalable, implicit parallel finite element framework, Olympus [24] on a Sun Constellation Linux Cluster (Ranger; Texas Advanced Computing Center, TX), for a total of 275 nonlinear analyses requiring around 50,000 CPU hours.

The main outcome of these analyses was the apparent-level yield strength in the longitudinal and transverse directions and, calculated from that, the biaxial yield point. For the uniaxial loading case, a strain offset of 0.2% on the stress-strain curve in the loading direction was used to define the apparent-level yield point; the percentage of yielded tissue was then calculated at this apparent-level yield point, as described elsewhere [23]. Correlations were calculated for both uniaxial yield strength and strain against bone volume fraction, elastic anisotropy, and various measures of microarchitecture (Table 1). Regression equations were then developed for the uniaxial yield strengths as a function of (when statistically significant) bone volume fraction, elastic anisotropy, and/or microarchitecture (Table 2). For each biaxial loading case, the individual stress-strain curves in the longitudinal and transverse directions were used to define the longitudinal and transverse yield points, respectively, using a 0.2% strain offset criterion on each curve. A single biaxial yield point (referred subsequently as the "chronological" yield point) was then defined by the biaxial stress state at the instant of first yielding in either the

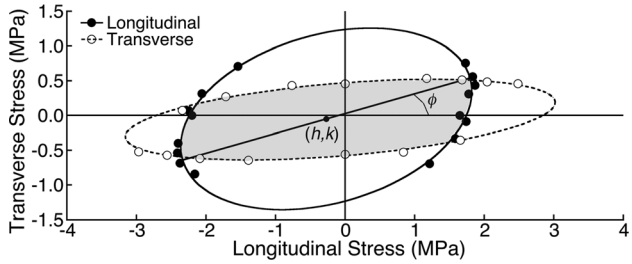

Fig. 2 The longitudinal (solid) and transverse (open) yield points and the respective yield ellipses for one specimen. Each ellipse is represented by five parameters, the major and minor diameters (*a* and *b*, respectively), the coordinates of the center (*h*,*k*), and the angle of tilt of the major axis with respect to the horizontal (ϕ). The shaded region bounded by the two intersecting ellipses defines the elastic region.

longitudinal or transverse direction (Fig. 1) as described elsewhere [10,12]. In this way, biaxial failure was defined as the first instant of failure in either the longitudinal or transverse loading directions. The percentage of yielded tissue was then calculated at the chronological biaxial yield point for each loading case.

A further analysis of the yield points was conducted to develop a mathematical description of the biaxial yield envelope expressed as a function of bone volume fraction, elastic anisotropy, and microarchitecture. This analysis involved two steps. First, for all 18–20 load cases for each specimen, we plotted both the finite element-computed yield points associated with each of the longitudinal and transverse loading directions, in the biaxial stress space, and fit a separate curve to the yield points associated with failure in each of the two loading directions. This analysis showed that a quadratic ellipse [25] worked well for failure associated with each individual loading direction (Fig. 2). The overall biaxial failure envelope was then taken as the inner surface created by each pair of longitudinal and transverse ellipses. For each specimen, the percentage error between the resulting fitted biaxial yield surface and the direct finite element-computed biaxial yield points was calculated using the difference of the vector norm of the biaxial stress from the origin [12], as follows,

$$\frac{\left\|\underline{\sigma}_{\text{predicted}} - \underline{\sigma}_{FE}\right\|}{\left\|\underline{\sigma}_{FE}\right\|} \times 100 \tag{1}$$

in which $\underline{\sigma}_{\text{predicted}}$ is the predicted yield point from the fitted ellipses and $\underline{\sigma}_{FE}$ is the finite element-computed yield point. This error per simulated biaxial test was then averaged over all simulated biaxial tests for each individual specimen, and the resulting mean error per specimen was then averaged over all specimens in order to assess how well the fitted biaxial failure criterion represented the direct finite element-generated biaxial failure points.

Second, to express the biaxial failure criterion as a function of bone volume fraction, elastic anisotropy, and the various microarchitecture parameters, each resulting in longitudinal and transverse ellipse for each individual specimen was characterized by five coefficients: the diameter of the major and minor axes (a, b), the shift of the center from the origin (h, k), and an angle of tilt with the longitudinal axis (ϕ) (Fig. 2); the equation of each ellipse is given by the equation

$$\left(\frac{2\sigma'_L}{a}\right)^2 + \left(\frac{2\sigma'_T}{b}\right)^2 = 1; \quad \begin{Bmatrix}\sigma'_L \\ \sigma'_T\end{Bmatrix} = \begin{bmatrix}\cos\phi & \sin\phi \\ -\sin\phi & \cos\phi\end{bmatrix} \begin{Bmatrix}\sigma_L - h \\ \sigma_T - k\end{Bmatrix} \tag{2}$$

in which σ_L and σ_T are the longitudinal and transverse stresses, respectively. We then calculated pairwise correlations of the five coefficients of the fitted ellipse with bone volume fraction, elastic anisotropy, and the various microarchitecture parameters (Table 1).

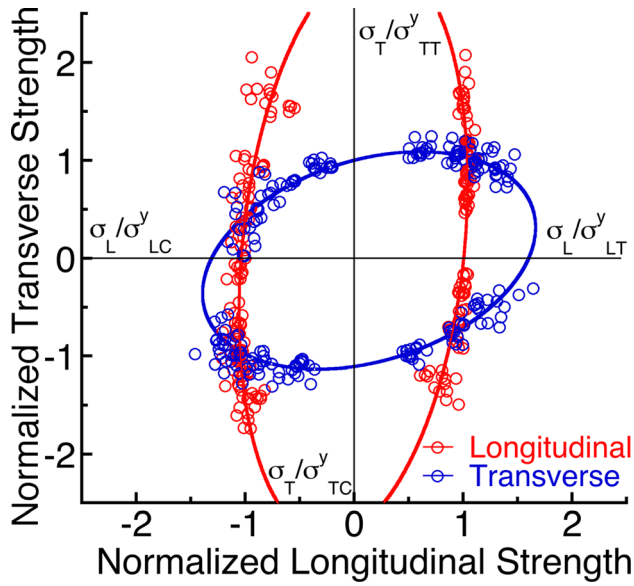

Fig. 3 A dual-ellipse fit to the normalized longitudinal and transverse yield strength data pooled from all specimens. The yield strength in each quadrant was normalized by the respective specimen-specific uniaxial strengths.

Table 3 Coefficients of the single ellipse, dual-ellipse, and quartic super-ellipse fits to the pooled normalized chronological yield strength data

	a	b	h	k	ϕ
Single Ellipse	2.70	2.08	0.0220	−0.0496	40.6
Dual Ellipse					
Longitudinal	5.94	2.04	−0.0065	0.1019	84.9
Transverse	3.19	2.03	0.1381	−0.0233	21.6

	c_L	c_T	r_L	r_T	t_L	t_T	ϕ
Quartic Super Ellipse	0.0014	−0.0547	1.05	1.42	0.84	1.98	102.9

To help better understand how bone volume fraction, anisotropy, and microarchitecture specifically influenced multiaxial behavior—as opposed to uniaxial behavior—we also developed a *stress-normalized criterion*, in which the biaxial strength was normalized by the uniaxial strength. To do so, for each specimen, the finite element-computed longitudinal and transverse yield points in each quadrant of the biaxial failure space were normalized by the respective finite element-computed uniaxial strengths for the specimen. For example, for a yield point in the longitudinal tension-transverse compression quadrant, all longitudinal strength values were divided by the uniaxial longitudinal tensile strength and all transverse strength values were divided by the transverse compressive strength of the specimen. A quadratic ellipse was then fit to these normalized longitudinal and transverse yield points (excluding the uniaxial points), and the five coefficients of each ellipse were calculated. Correlation analysis was then used to relate the five coefficients of the fitted normalized ellipses to bone volume fraction, elastic anisotropy, and the various microarchitecture parameters (Table 1). This was done for each individual specimen. Further, the normalized longitudinal and transverse yield points from all specimens were pooled together in a single plot and a quadratic ellipse was fit to each of the pooled normalized longitudinal and transverse yield points (referred subsequently as the "dual-ellipse" yield surface, Fig. 3). Using Eq. (1), a percentage error was calculated between the dual-ellipse yield surface and the pooled normalized longitudinal, transverse, and chronological yield points.

To facilitate comparison with the literature, two additional fits were performed on the pooled normalized chronological yield points (Fig. 4, Table 3)—a single quadratic ellipse as described in Eq. (2) and a quartic super-ellipse similar to the modified super-ellipsoid equation reported by Bayraktar et al. [12]

$$\left(\frac{\hat{\sigma}'_L}{r_L}\right)^4+\left(\frac{\hat{\sigma}'_T}{r_T}\right)^4+\left(\frac{t_L\hat{\sigma}'_L+t_T\hat{\sigma}'_T}{r_L+r_T}\right)^4=1$$
$$\begin{Bmatrix}\hat{\sigma}'_L\\ \hat{\sigma}'_T\end{Bmatrix}=\begin{bmatrix}\cos\phi & \sin\phi\\ -\sin\phi & \cos\phi\end{bmatrix}\begin{Bmatrix}\hat{\sigma}_L-c_L\\ \hat{\sigma}_T-c_T\end{Bmatrix} \quad (3)$$

in which $\hat{\sigma}_L$ and $\hat{\sigma}_T$ are the normalized longitudinal and transverse stresses, respectively, and c_L, c_T, t_L, t_T, r_L, r_T, and ϕ are parameters of the equation. Using Eq. (1), a percentage error was calculated between the finite element-computed normalized chronological yield points and the corresponding predictions from the dual-ellipse yield surface, single-ellipse surface, and the quartic super-ellipse surface. To explore the sensitivity of the biaxial yield strength to an alternate definition of yielding, we calculated the yield point based on an "equivalent" stress-strain curve as reported elsewhere [14]. Briefly, the individual stress-strain response in the longitudinal and transverse directions from each analysis were used to calculate an equivalent stress and equivalent strain response. The equivalent stress or strain was defined as the square root of the double inner product of the stress or strain tensor respectively [14]. The yield point was calculated based on a 0.2% strain offset on the equivalent stress-strain response and the longitudinal and transverse stresses at the yield point defined the "equivalent" yield point. The "equivalent" yield data from all analyses were normalized with the respective uniaxial strengths of each specimen and the pooled data from all specimens were plotted together (Fig. 5); a single quadratic ellipse was also fit to the pooled equivalent yield data and was compared with the dual-ellipse surface.

Finally, to gain insight into specific characteristics of the biaxial failure behavior, the normalized dual-ellipse yield surface,

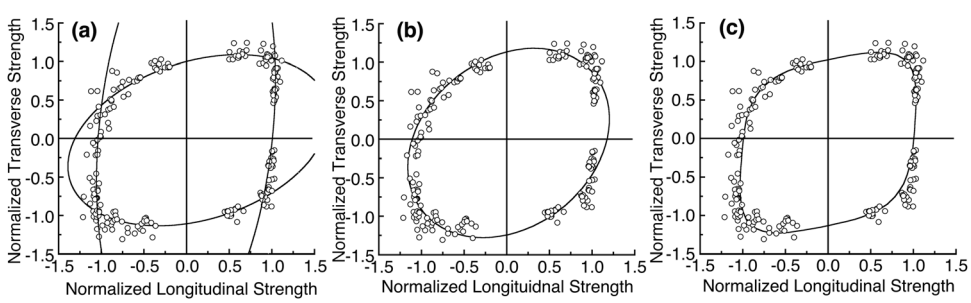

Fig. 4 (*a*) Dual-ellipse fit, (*b*) single-ellipse fit, and (*c*) quartic super-ellipse fit to the (same) pooled normalized chronological yield strength data

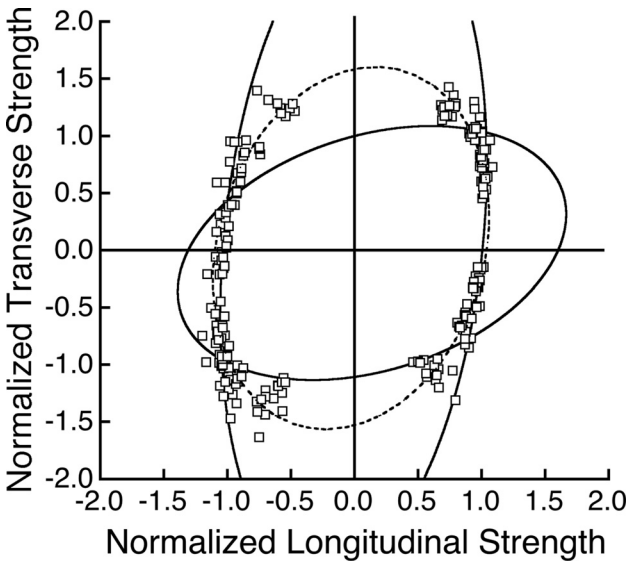

Fig. 5 Comparison of dual-ellipse fit (solid) and a quadratic fit (dotted) to the pooled normalized "equivalent" yield strength data

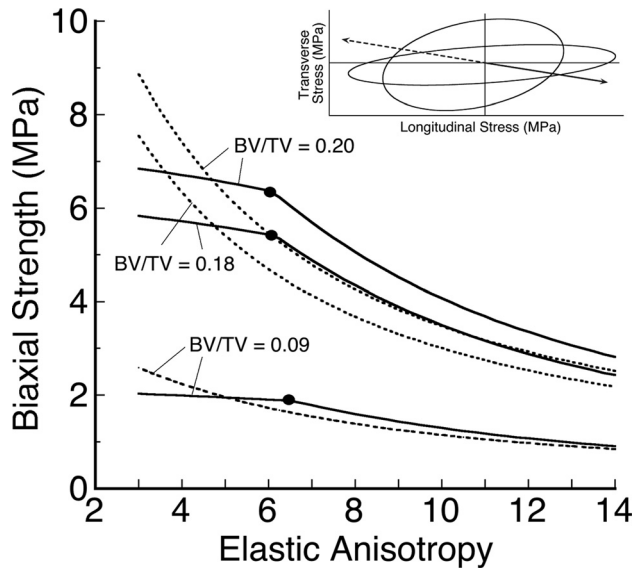

Fig. 6 Variation of biaxial strength with elastic anisotropy at a constant bone volume fraction (BV/TV) of 0.09, 0.18, and 0.20 for two biaxial loading cases: longitudinal compression and transverse tension in a ratio of 5:1 (dotted line); and longitudinal tension and transverse compression, also in a ratio of 5:1 (solid line). For longitudinal compression and transverse tension, biaxial strength was always defined by the transverse direction. However, for longitudinal tension and transverse compression, the biaxial strength was defined by the longitudinal direction up to an elastic anisotropy of ~6, beyond which the biaxial strength was defined by the transverse direction, leading to a change in the relation between biaxial strength and elastic anisotropy.

coupled with its underlying regressions between uniaxial strength and bone volume fraction and elastic anisotropy, were used to calculate the biaxial strength as a function of elastic anisotropy, for three constant values of bone volume fraction, all done for two relevant biaxial loading cases. The tissue-level yielding for these two loading cases was investigated for three femoral specimens, two from the femoral neck and one from the greater trochanter.

3 Results

For each specimen, the yield surface in the biaxial stress space, as computed by the finite element analyses, was well represented by the combination of the longitudinal and transverse ellipses (Fig. 2). Across all 15 specimens, the mean (±SD) error between the finite element-computed yield points for the longitudinal loading direction and the fitted longitudinal ellipse was $2.9 \pm 0.7\%$; for the transverse loading direction, the corresponding error was $3.3 \pm 0.7\%$. As expected, the major and minor diameters of the ellipses (a,b) increased with increasing bone volume fraction (Table 1). We also found that the minor diameters (b) decreased with increasing elastic anisotropy and, therefore, the aspect ratio (a/b) increased with elastic anisotropy. In addition, the angle of tilt (ϕ) of the ellipses decreased with increasing elastic anisotropy asymptotically, tending to zero for highly anisotropic specimens. The elastic anisotropy was not correlated with bone volume fraction ($p = 0.20$) and was only weakly correlated with the morphological degree of anisotropy (DA) ($r = 0.50$, $p = 0.06$).

For uniaxial loading, the longitudinal yield strength was correlated to bone volume fraction while the transverse yield strength was correlated to both bone volume fraction and elastic anisotropy (Table 1). Power law regressions described well the variation in uniaxial strength when bone volume fraction and/or elastic anisotropy served as the independent variables; microarchitecture did not provide any additional statistical association (Table 2). Consistent with results from prior experiments [15,16,26,27], the yield strain for longitudinal compression increased with bone volume fraction ($r = 0.80$, $p = 0.0003$) but for transverse compression did not ($p = 0.22$).

As a result of these similar associations for uniaxial yield strengths and the various coefficients of the longitudinal and transverse yield ellipses, the coefficients of the normalized longitudinal and transverse yield ellipses depended only weakly on bone volume fraction, elastic anisotropy, or microarchitecture (Table 1). This weak dependence was also evident in the small amount of scatter in the normalized longitudinal and transverse yield data pooled from all specimens (Fig. 3), indicating that the residual variations in the biaxial strength were minor after accounting for the variations in uniaxial strength. This set of pooled normalized longitudinal and transverse yield data from all specimens was well described by a single dual-ellipse yield surface (Fig. 3, Table 3), which had a mean (±SD) error of $3.9 \pm 1.7\%$ and $6.1 \pm 2.5\%$ for the fitted normalized longitudinal and transverse ellipses, respectively. The pooled normalized (chronological) yield points was best described by the dual-ellipse yield surface (Fig. 4(*a*), mean ± SD error = $4.8 \pm 4.1\%$), followed by the quartic-superellipse yield surface (Fig. 4(*b*), mean ± SD error = $5.2 \pm 4.2\%$) and then the single-ellipse yield surface (Fig. 4(*c*), mean ± SD error = $6.5 \pm 4.6\%$).

While the pooled equivalent yield data was quite well described a quadratic ellipse with a mean error of $4.9 \pm 4.4\%$, this formulation did not capture the complete biaxial behavior (Fig. 5). For a biaxial loading with a high proportion of longitudinal loading, the equivalent yield points were close to the longitudinal ellipse. However, the quadratic ellipse substantially overpredicted the transverse tensile and compressive uniaxial strengths. As a result, for biaxial loading with a high proportion of transverse loading, the equivalent yield points lay between the longitudinal and transverse yield ellipses (Fig. 5).

The normalized dual-ellipse yield surface, coupled with the regressions on uniaxial strength, revealed that the biaxial yield strength for two biaxial compression-tension loading scenarios decreased with increasing elastic anisotropy, independent of the bone volume fraction (Fig. 6). For a longitudinal compression and transverse tension biaxial loading having a ratio of ~5, the biaxial apparent yield point was determined by the transverse response for all three specimens. Visual inspection revealed that for this loading case, there was predominantly tensile failure of the

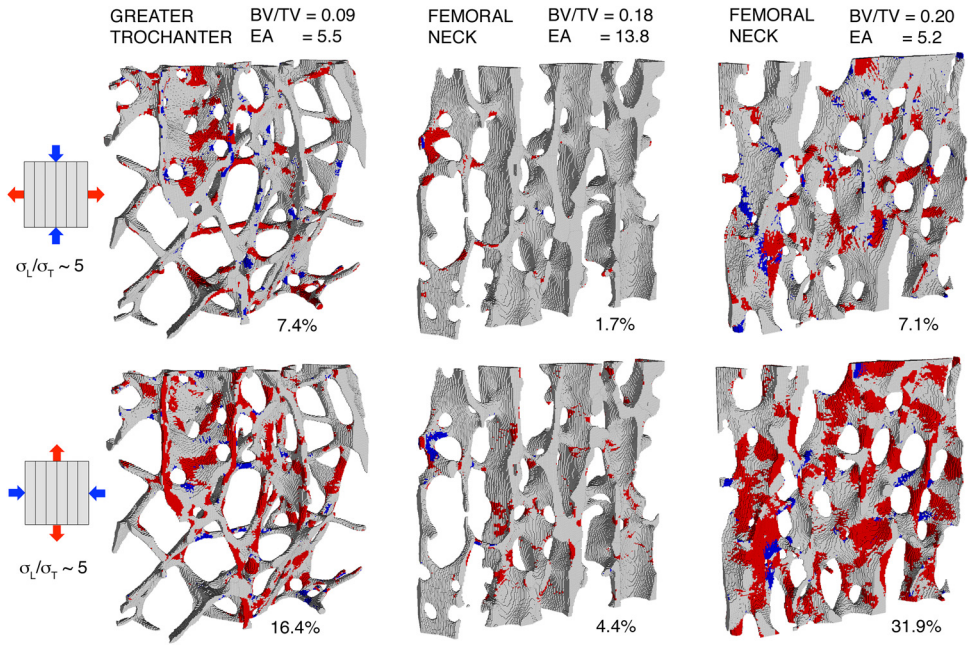

Fig. 7 Distribution of yielded tissue at the biaxial yield point in thin (~0.45 mm) longitudinal slices taken from three 5 mm cube specimens subjected to two biaxial loading cases (top row: longitudinal compression and transverse tension in a ratio of about 5:1; bottom row: longitudinal tension and transverse compression, also in a ratio of about 5:1). The percentage value denotes the proportion (percentage) of total tissue yielded in the overall cube specimen at the biaxial yield point. Red regions denote tissue yielded in tension and blue regions denote tissue yielded in compression. BV/TV = bone volume fraction; EA = elastic anisotropy. (The reader is referred to the online version of this article (doi:10.1115/1.4025679) for interpretation of the references to color.)

horizontally oriented trabeculae (Fig. 7) for all three specimens. Of the two femoral neck specimens having a similar bone volume fraction, the more anisotropic specimen sustained much less tissue-level failure at the overall biaxial failure point. By contrast, for longitudinal tension and transverse compression in a ratio of ~5, the direction determining the biaxial yield point depended on anisotropy. For example, for the highly anisotropic femoral neck specimen, the transverse direction yielded first whereas for the two less anisotropic specimens, the longitudinal direction yielded first. This is consistent with the observation that the biaxial failure mode, for this particular biaxial loading, changed from the longitudinal to the transverse direction above an elastic anisotropy of around 6.0 (Fig. 6). Visual inspection revealed that for this type of biaxial loading, there was predominantly tensile tissue failure for all specimens. This failure distribution was primarily distributed in the longitudinally oriented trabeculae for the less anisotropic specimens and equally distributed between the longitudinally and horizontally oriented trabeculae for the highly anisotropic specimen (Fig. 7).

4 Discussion

The results of this computational analysis suggest that the biaxial yield behavior of human trabecular bone, in the axial-transverse plane, can be described well by a dual-ellipse surface, the size of which depends primarily on bone volume fraction whereas the shape (i.e., aspect ratio) and orientation of which depend primarily on elastic anisotropy. This dependence of biaxial yield strength on bone volume fraction and elastic anisotropy can be primarily attributed to a similar dependence of the uniaxial yield strengths on bone volume fracture and elastic anisotropy, resulting in relatively little unexplained inter-specimen variation of biaxial yield behavior after accounting for the uniaxial yield behavior. Using parametric study of this normalized failure criterion, expressed as a function of the bone volume fraction and elastic anisotropy, we found that, independent of bone volume fraction, an increase in the elastic anisotropy, which is primarily associated with a decrease in transverse strength, leads to a simultaneous increase in aspect ratio and decrease in orientation of the biaxial yield surface, which together reduce biaxial strength by making the specimen more susceptible to failure in the weaker transverse direction.

One advantage of performing such investigations using high-resolution, specimen-specific finite element simulation is that insight can be obtained into the underlying failure mechanisms, which would be difficult to achieve by experimentation. For example, under a combined longitudinal-compression and transverse-tension biaxial loading, as might typically occur in the proximal femur during gait [1], we found that trabecular bone is likely to yield first due to failure associated with the transverse tensile loading component because of predominant failure at the tissue level of the horizontally oriented trabeculae via tensile failure (bone tissue is particularly weak in tension). However, for a combined longitudinal-tension and transverse-compression biaxial loading, as might typically occur in the proximal femur during a sideways fall [2], the microstructurally weaker direction (transverse) is now loaded in the stronger tissue-failure mode (compression), and the microstructurally stronger direction (longitudinal) is loaded in the weaker tissue-failure mode (tension). Therefore, the apparent-level yield can occur either in the longitudinal or transverse direction, depending on the degree of mechanical anisotropy of the specimen. For a less anisotropic specimen, the apparent-level yield points in the longitudinal and transverse directions are similar, but for a highly anisotropic specimen, we found that apparent-level yield occurs first in the transverse direction. Further, in a highly anisotropic specimen, since there are proportionately fewer and thinner horizontally oriented trabeculae [5,28,29], the trabecular microstructure can sustain only a small amount of tissue failure

before overall apparent-level yield in the transverse direction. Therefore, in the context of osteoporosis, under the biaxial loading of the trabecular bone within the proximal femur that might typically occur during a sideways fall, for a given bone volume fracture, a specimen having increased mechanical anisotropy can be susceptible to premature yield in the nonprimary loading direction. This mechanism might help explain results from previous studies showing that when matched for bone volume fracture, patients with hip fractures had a more anisotropic trabecular microstructure compared to nonfracture controls [5,7].

The results from these biaxial simulations also lend insight into off-axis behavior, specifically, why 45 deg off-axis compressive yield strains do not depend on bone volume fraction although on-axis longitudinal compressive yield strains do [15]. According to the principles of stress tensor transformation, a 45 deg off-axis compression at a normal stress σ is equivalent to a combination of an on-axis longitudinal compression-transverse compression equibiaxial normal loading at stress $\sigma/2$ and a shear loading at stress $\tau = \sigma/2$. Since yielding under equibiaxial normal loading will always occur in the transverse direction (Fig. 2), the yielding under the equibiaxial normal component of the off-axis loading should be dominated by failure associated with on-axis transverse compression. The results from our earlier work [23], together with the data in Table 2, show that the on-axis transverse compressive strength is about equal to or much lower than the shear strength, depending on the degree of anisotropy. Therefore, the failure during 45 deg off-axis compressive loading should occur primarily via compression failure in the (on-axis) transverse direction. In that event, since the on-axis transverse compressive yield strain does not depend on bone volume fraction, the 45 deg off-axis compressive yield strain should likewise not depend on bone volume fraction.

Our new results are consistent with previous studies that have defined the multiaxial failure envelope for trabecular bone as an intersection of multiple surfaces as opposed to just a single quadratic-type surface. Our yield envelope consisting of two intersecting ellipses in stress space is similar to what has been proposed previously for bovine bone in strain space, based on micro-CT-based finite element analysis [11]. Two intersecting ellipses have also been used to define a failure envelope for cellular solids [30] under biaxial loading, based on assumptions of the plastic collapse of cell walls as the primary failure mode, while others also proposed two separate ellipsoidal envelopes based on a generalized Hill's failure criterion [31]. Alternatively, the inner surface of the two intersecting ellipses can be defined by a super-ellipsoid equation as done previously for human femoral bone in strain space [12]. The equation employed in the current study is similar in form to the modified super-ellipsoid equation [12] but with the exponents enforced to equal a value of 4.0 and an additional parameter introduced to quantify the angle of tilt. The angle of tilt is introduced since the biaxial yield was defined in stress space as opposed to strain space in the previous study [12]. While both strain- and stress-based criteria can be incorporated into computational models, we are reporting the criterion in stress space since a stress-based criterion facilitates direct comparison with multiaxial experiments because it is not necessary to measure any Poisson effects. We also observed that the angle of tilt of the yield ellipses varies with elastic anisotropy, which is consistent with previous studies on fiber-reinforced composite materials [32] that have suggested the angle of tilt is a function of anisotropy.

One prominent question concerning multiaxial behavior of human trabecular bone remains whether the yield behavior can be described by the quadratic Tsai–Wu criterion. A recent study [14], specifically addressing the failure behavior of human vertebral trabecular bone, used Cowin's [8] type of formulation to propose a single Tsai–Wu ellipsoidal criterion as a function of both bone volume fraction and fabric based anisotropy. However, that study calibrated data generated from finite element simulations using just a few loading cases and as such did not have a sufficient number of degrees of freedom to detect more complex behavior. In a previous study on tri-axial compressive behavior of bovine trabecular bone, it was found that although one can indeed calibrate a single Tsai–Wu quadratic yield envelope to triaxial data, the resulting fit was not general and, therefore, did not work well for altered loading conditions [9]. Alternatively, as shown here, the yield surface could be well described by a quartic super-ellipse equation. That yield surface has boxlike shape, which is also supported by theoretical and experimental studies on open-cell foams [30,33]. In the normalized stress space, we observed that the angle of tilt of the longitudinal ellipse is close to 90 deg, which suggests that failure responses in the longitudinal direction occur around a constant principal stress. On the other hand, the transverse ellipse had an angle of tilt of 22 deg, which, at about halfway between 0 deg and 45 deg, suggests that failure in the transverse direction is somewhere between a principal stress type failure and quadratic von Mises type failure (the angle of tilt for a von Mises yield equation is 45 deg). Taken together, these results, therefore, suggest that the biaxial failure of human trabecular bone in the axial-transverse plane, like other porous microstructured materials [34], is not entirely quadratic.

One unique challenge in comparing different multiaxial failure criteria across studies is to account for the failure in the multiple different loading directions. While in this study we chose to define the apparent—level yield point based on two individual stress—strain curves in the longitudinal and transverse directions as done previously in other studies [10–12], Wolfram et al. [14] defined the apparent-level yield point based on an "equivalent" stress-strain curve constructed from the components of the stress and strain tensor. Similarly, other studies on multiaxial behavior of cortical bone [35], cellular solids [36], and polymers [37] have used "equivalent" stress and/or strain definitions to define a composite-type yield point under multiaxial loading. Our results show that while the "equivalent" approach works well for a biaxial loading having a high proportion of longitudinal loading, such biaxial yield points are overestimated when there is substantial transverse loading (Fig. 5). This is reflected in a 50% over-prediction of the uniaxial transverse yield strengths from the elliptical fit to the equivalent yield points (Fig. 5). Using the chronological yield definition leads to only a minor over-prediction of uniaxial compressive yield strengths, which is likely due to unavoidable edge-effects of unconnected trabeculae on the boundary [38]. Under predominantly longitudinal loading, the transverse stress is negligible due to the anisotropic nature of trabecular bone and, therefore, the biaxial equivalent stress-strain response closely resembles the uniaxial longitudinal stress-strain response. However, under a more predominantly transverse type of biaxial loading, the magnitude of transverse stress becomes comparable to the magnitude of longitudinal stress, and therefore, the equivalent yield point lies somewhere between the yield points obtained from the longitudinal and transverse directions individually. The use of two separate stress-strain responses, one for each principal material direction, while mathematically more complex is more mechanistic in nature and allows one to interpret the mode of apparent-level yield in either the longitudinal or transverse trabecular orientation.

While we assumed trabecular bone to behave as a transversely isotropic material as assumed in previous studies [9,14], its behavior is truly orthotropic [39]. The large scatter and error observed in elliptical fit in the transverse direction can be possibly explained by the random choice of the transverse direction. If we assume a significant difference in the elastic moduli in the two transverse directions, the observed scatter in the normalized chronological yield data can vary depending on the choice of the transverse plane, which may lead to higher or lower error estimates of the proposed dual-ellipse yield surface. It would be worthwhile to further explore the yield behavior in other planes and include other loadings such as shear loading in order to obtain a more complete picture of the multiaxial yield behavior. We also allowed an angle of misalignment of up to 10 deg in the trabecular bone specimens, which can induce an error of up to 9.5% in the measurement of the elastic moduli [39]. While it is difficult to get

specimens that are perfectly aligned with the principal material coordinate system, the error due to this misalignment is of the same magnitude as the error in the uniaxial strength predictions with power law regressions on bone volume fraction. Therefore, we assumed the misalignment of 10 deg or less adequately represents the elastic anisotropy of the trabecular bone specimens.

Our study has some additional limitations. First, at the tissue level we considered only plastic yielding and kinematically nonlinear "large deformations" as the failure mechanism under all biaxial loading modes. Based on cellular solid theory, different failure mechanisms such as brittle cracking under tension can lead to different failure envelopes under biaxial loading [30,40]. While our elastic-plastic constitutive model was shown to give good agreement for both apparent-level and tissue-level yield for longitudinal compression loading [23], there remains a need to investigate more sophisticated tissue-level constitutive models in these types of multiaxial computational studies since bone tissue material properties may change with age and disease, and the degree of ductility is not unlimited [41–43]. Second, we considered the bone tissue to be homogeneous and isotropic. The material anisotropy of the bone tissue likely only has a small influence on the overall anisotropy of trabecular bone at the apparent level since the apparent level anisotropy is primarily due to the trabecular structure [44–46] (i.e., structural anisotropy). Likewise, the effects of mineral heterogeneity on the apparent behavior should be also minor [47,48]. Third, we used displacement boundary conditions for generating the biaxial stress states in our finite element simulations. This may provide an upper bound on the effective biaxial strength whereas use of force boundary conditions may provide a lower bound on the effective biaxial strength [49]. However, the effect of bone volume fraction and anisotropy should still reflect on the size, shape, and orientation of the yield ellipses irrespective of the boundary condition used. Finally, it should be appreciated that all our biaxial results were generated from computational analyses, and, despite the excellent performance of these finite element simulations for uniaxial strength behavior [23], definitive validation for biaxial behavior can only come from additional experiments.

Acknowledgment

Funding was provided by the National Institutes of Health (NIH AR43784). Cadaveric material was supplied by the Anatomic Gift Foundation and NDRI. Micro-CT imaging was performed by Andrew Burghardt at UC San Francisco. Supercomputer resources were obtained from the National Science Foundation's Extreme Science and Engineering Discovery Environment (XSEDE) project. We would like to thank SkyScan, Belgium for providing the CTAn software.

References

[1] van Rietbergen, B., Huiskes, R., Eckstein, F., and Rüegsegger, P., 2003, "Trabecular Bone Tissue Strains in the Healthy and Osteoporotic Human Femur," J. Bone Miner. Res., **18**(10), pp. 1781–1788.
[2] Verhulp, E., van Rietbergen, B., and Huiskes, R., 2008, "Load Distribution in the Healthy and Osteoporotic Human Proximal Femur During a Fall to the Side," Bone, **42**(1), pp. 30–35.
[3] Homminga, J., van Rietbergen, B., Lochmuller, E. M., Weinans, H., Eckstein, F., and Huiskes, R., 2004, "The Osteoporotic Vertebral Structure is Well Adapted to the Loads of Daily Life, but not to Infrequent 'Error' Loads," Bone, **34**(3), pp. 510–516.
[4] Newitt, D. C., Majumdar, S., van Rietbergen, B., von Ingersleben, G., Harris, S. T., Genant, H. K., Chesnut, C., Garnero, P., and MacDonald, B., 2002, "In Vivo Assessment of Architecture and Micro-Finite Element Analysis Derived Indices of Mechanical Properties of Trabecular Bone in the Radius," Osteoporosis Int., **13**(1), pp. 6–17.
[5] Ciarelli, T. E., Fyhrie, D. P., Schaffler, M. B., and Goldstein, S. A., 2000, "Variations in Three-Dimensional Cancellous Bone Architecture of the Proximal Femur in Female Hip Fractures and in Controls," J. Bone Miner. Res., **15**(1), pp. 32–40.
[6] Tanck, E., Bakker, A. D., Kregting, S., Cornelissen, B., Klein-Nulend, J., and van Rietbergen, B., 2009, "Predictive Value of Femoral Head Heterogeneity for Fracture Risk," Bone, **44**(4), pp. 590–595.
[7] Homminga, J., McCreadie, B. R., Ciarelli, T. E., Weinans, H., Goldstein, S. A., and Huiskes, R., 2002, "Cancellous Bone Mechanical Properties From Normals and Patients With Hip Fractures Differ on the Structure Level, Not on the Bone Hard Tissue Level," Bone, **30**(5), pp. 759–764.
[8] Cowin, S. C., 1986, "Fabric Dependence of an Anisotropic Strength Criterion," Mech. Mater., **5**, pp. 251–260.
[9] Keaveny, T. M., Wachtel, E. F., Zadesky, S. P., and Arramon, Y. P., 1999, "Application of the Tsai-Wu Quadratic Multiaxial Failure Criterion to Bovine Trabecular Bone," ASME J. Biomech. Eng., **121**(1), pp. 99–107.
[10] Fenech, C. M., and Keaveny, T. M., 1999, "A Cellular Solid Criterion for Predicting the Axial-Shear Failure Properties of Trabecular Bone.," ASME J. Biomech. Eng., **121**(4), pp. 414–422.
[11] Niebur, G. L., Feldstein, M. J., and Keaveny, T. M., 2002, "Biaxial Failure Behavior of Bovine Tibial Trabecular Bone," ASME J. Biomech. Eng., **124**(6), pp. 699–705.
[12] Bayraktar, H. H., Gupta, A., Kwon, R. Y., Papadopoulos, P., and Keaveny, T. M., 2004, "The Modified Super-Ellipsoid Yield Criterion for Human Trabecular Bone," ASME J. Biomech. Eng., **126**(6), pp. 677–684.
[13] Rincon-Kohli, L., and Zysset, P. K., 2009, "Multi-Axial Mechanical Properties of Human Trabecular Bone," Biomech. Model. Mechanobiol., **8**(3), pp. 195–208.
[14] Wolfram, U., Gross, T., Pahr, D. H., Schwiedrzik, J., Wilke, H. J., and Zysset, P. K., 2012, "Fabric-Based Tsai-Wu Yield Criteria for Vertebral Trabecular Bone in Stress and Strain Space," J. Mech. Behav. Biomed. Mater., **15**, pp. 218–228.
[15] Bevill, G., Farhamand, F., and Keaveny, T. M., 2009, "Heterogeneity of Yield Strain in Low-Density Versus High-Density Human Trabecular Bone," J. Biomech., **42**(13), pp. 2165–2170.
[16] Morgan, E. F., and Keaveny, T. M., 2001, "Dependence of Yield Strain of Human Trabecular Bone on Anatomic Site," J. Biomech., **34**(5), pp. 569–577.
[17] Rüegsegger, P., Koller, B., and Müller, R., 1996, "A Microtomographic System for the Nondestructive Evaluation of Bone Architecture," Calcif. Tissue Int., **58**(1), pp. 24–29.
[18] Beck, J. D., Canfield, B. L., Haddock, S. M., Chen, T. J., Kothari, M., and Keaveny, T. M., 1997, "Three-Dimensional Imaging of Trabecular Bone Using the Computer Numerically Controlled Milling Technique," Bone, **21**(3), pp. 281–287.
[19] Hildebrand, T., Laib, A., Müller, R., Dequeker, J., and Rüegsegger, P., 1999, "Direct Three-Dimensional Morphometric Analysis of Human Cancellous Bone: Microstructural Data From Spine, Femur, Iliac Crest, and Calcaneus," J. Bone Miner. Res., **14**(7), pp. 1167–1174.
[20] van Rietbergen, B., Odgaard, A., Kabel, J., and Huiskes, R., 1996, "Direct Mechanics Assessment of Elastic Symmetries and Properties of Trabecular Bone Architecture," J. Biomech., **29**(12), pp. 1653–1657.
[21] Papadopoulos, P., and Lu, J., 2001, "On the Formulation and Numerical Solution of Problems in Anisotropic Finite Plasticity," Comput. Methods Appl. Mech. Eng., **190**(37–38), pp. 4889–4910.
[22] Bevill, G., Eswaran, S. K., Gupta, A., Papadopoulos, P., and Keaveny, T. M., 2006, "Influence of Bone Volume Fraction and Architecture on Computed Large-Deformation Failure Mechanisms in Human Trabecular Bone.," Bone, **39**(6), pp. 1218–1225.
[23] Sanyal, A., Gupta, A., Bayraktar, H. H., Kwon, R. Y., and Keaveny, T. M., 2012, "Shear Strength Behavior of Human Trabecular Bone," J. Biomech., **45**(15), pp. 2513–2519.
[24] Adams, M. F., Bayraktar, H. H., Keaveny, T. M., and Papadopoulos, P., 2004, "Ultrascalable Implicit Finite Element Analyses in Solid Mechanics With Over a Half a Billion Degrees of Freedom," Proceedings of the ACM/IEEE SC2004: High Performance Networking and Computing.
[25] Fitzgibbon, A. M. P., and Fisher, B., 1999, "Direct Least-Squares Fitting of Ellipses," IEEE Trans. Pattern Anal. Mach. Intell., **21**(5), pp. 476–480.
[26] Kopperdahl, D. L., and Keaveny, T. M., 1998, "Yield Strain Behavior of Trabecular Bone," J. Biomech., **31**(7), pp. 601–608.
[27] Chang, W. C. W., Christensen, T. M., Pinilla, T. P., and Keaveny, T. M., 1999, "Isotropy of Uniaxial Yield Strains for Bovine Trabecular Bone," J. Orthop. Res., **17**, pp. 582–585.
[28] Mosekilde, L., 1988, "Age-Related Changes in Vertebral Trabecular Bone Architecture—Assessed by a New Method," Bone, **9**(4), pp. 247–250.
[29] Thomsen, J. S., Ebbesen, E. N., and Mosekilde, L., 2002, "Age-Related Differences Between Thinning of Horizontal and Vertical Trabeculae in Human Lumbar Bone as Assessed by a New Computerized Method," Bone, **31**(1), pp. 136–142.
[30] Gibson, L. J., Ashby, M. F., Zhang, J., and Triantafillou, T. C., 1989, "Failure Surfaces for Cellular Materials Under Multiaxial Loads-I. Modelling," Int. J. Mech. Sci., **31**(9), pp. 635–663.
[31] Zysset, P. K., and Rincon-Kohli, L., 2006, "An Alternative Fabric-Based Yield and Failure Criterion for Trabecular Bone," *Mechanics of Bilogical Tissue*, G. A. Holzapfel and R. W. Ogden, eds., Springer, New York, pp. 457–470.
[32] Wu, R., and Stachurski, Z., 1984, "Evaluation of the Normal Stress Interaction Parameter in the Tensor Polynomial Strength Theory for Anisotropic Materials," J. Compos. Mater., **18**, pp. 456–463.
[33] Traintafillou, T. C., Zhang, J., Shercliff, T. L., Gibson, L. J., and Ashby, M. F., 1989, "Failure Surfaces for Cellular Materials Under Multiaxial Loads. II. Comparison of Models With Experiment," Int. J. Mech. Sci., **31**(9), pp. 665–678.
[34] Wang, D.-A., and Pan, J., 2006, "A Non-Quadratic Yield Function for Polymeric Foams," Int. J. Plast., **22**, pp. 434–458.
[35] Cezayirlioglu, H., Bahniuk, E., Davy, D. T., and Heiple, K. G., 1985, "Anisotropic Yield Behavior of Bone Under Combined Axial Force and Torque," J. Biomech., **18**(1), pp. 61–69.
[36] Gioux, G., McCormack, T. M., and Gibson, L. J., 2000, "Failure of Aluminum Foams Under Multiaxial Loads," Int. J. Mech. Sci., **42**, pp. 1097–1117.

[37] Rottler, J., and Robbins, M. O., 2001, "Yield Conditions for Deformation of Amorphous Polymer Glasses," Phys. Rev. E, **64**, p. 051801.
[38] Brezny, R., and Green, D. J., 1990, "Characterization of Edge Effects in Cellular Materials," J. Mater. Sci., **25**(11), pp. 4571–4578.
[39] Turner, C. H., and Cowin, S. C., 1988, "Errors Introduced by Off-Axis Measurements of the Elastic Properties of Bone," J. Biomech., **110**, pp. 213–214.
[40] Triantafillou, T. C., and Gibson, L. J., 1990, "Multiaxial Failure Criteria for Brittle Foams," Int. J. Mech. Sci., **32**(6), pp. 479–496.
[41] Burr, D. B., 2002, "The Contribution of the Organic Matrix to Bone's Material Properties," Bone, **31**(1), pp. 8–11.
[42] Milovanovic, P., Potocnik, J., Djonic, D., Nikolic, S., Zivkovic, V., Djuric, M., and Rakocevic, Z., 2012, "Age-Related Deterioration in Trabecular Bone Mechanical Properties at Material Level: Nanoindentation Study of the Femoral Neck in Women by Using AFM," Exp. Gerontol., **47**(2), pp. 154–159.
[43] Nawathe, S., Juillard, F., and Keaveny, T. M., 2013, "Theoretical Bounds for the Influence of Tissue-Level Ductility on the Apparent-Level Strength of Human Trabecular Bone," J. Biomech., **46**(7), pp. 1293–1299.
[44] Kabel, J., van Rietbergen, B., Dalstra, M., Odgaard, A., and Huiskes, R., 1999, "The Role of an Effective Isotropic Tissue Modulus in the Elastic Properties of Cancellous Bone," J. Biomech., **32**(7), pp. 673–680.
[45] Hou, F. J., Lang, S. M., Hoshaw, S. J., Reimann, D. A., and Fyhrie, D. P., 1998, "Human Vertebral Body Apparent and Hard Tissue Stiffness," J. Biomech., **31**(11), pp. 1009–1015.
[46] Cowin, S., ed., 2001, *Bone Mechanics Handbook*, CRC Press, Boca Raton, FL.
[47] Gross, T., Pahr, D. H., Peyrin, F., and Zysset, P. K., 2012, "Mineral Heterogeneity has a Minor Influence on the Apparent Elastic Properties of Human Cancellous Bone: a SRμCT-Based Finite Element Study," Comput. Methods Biomech. Biomed. Eng., **15**(11), pp. 1137–1144.
[48] Easley, S. K., Jekir, M. G., Burghardt, A. J., Li, M., and Keaveny, T. M., 2010, "Contribution of the Intra-Specimen Variations in Tissue Mineralization to PTH- and Raloxifene-Induced Changes in Stiffness of Rat Vertebrae," Bone, **46**(4), pp. 1162–1169.
[49] Wang, C., Feng, L., and Jasiuk, I., 2009, "Scale and Boundary Conditions Effects on the Apparent Elastic Moduli of Trabecular Bone Modeled as a Periodic Cellular Solid," ASME J. Biomech. Eng., **131**(12), p. 121008.